Chapter 4

Optical Vortices Illumination Enables the Creation of Chiral Nanostructures

Takashige Omatsu, Katsuhiko Miyamoto and Ryuji Morita

Additional information is available at the end of the chapter

http://dx.doi.org/10.5772/67073

Abstract

We discovered that optical vortices with an annular spatial form and an orbital angular momentum owing to a helical wave front enable us to twist materials, such as metal, silicon and azo-polymer, to form various structured matters including microneedles, chiral nanostructures and chiral surface reliefs. Such structured matters will potentially open the door to advanced devices, for instance, silicon photonic device, biomedical micro-electro-mechanical systems, ultrasensitive detector for chiral chemical composites and plasmonic metasurfaces for chiral chemical reactions.

Keywords: singular optics, optical vortices, orbital angular momentum, laser materials processing, chiral structured materials

1. Introduction

Optical vortices [1–3] carry an annular spatial form and an orbital angular momentum (l) owing to an associated helical wave front with phase singularity $l\phi$ (where l is an integer and ϕ is the azimuthal angle) (**Figure 1**) and they have widely received much attention in a variety of fields, such as optical trapping and manipulations [4–6], space division multiplexing optical telecommunications [7, 8], quantum physics [9] and "super-resolution" microscopes with a spatial resolution beyond the diffraction limit [10–12].

In recent years, we discovered that optical vortices enable us to twist various materials, for example, metal, silicon and azo-polymer, so as to form a variety of structured matters including microneedles, chiral nanostructures and chiral surface reliefs. Such structured matters created by optical vortex illumination will potentially open the door to various material sciences and for

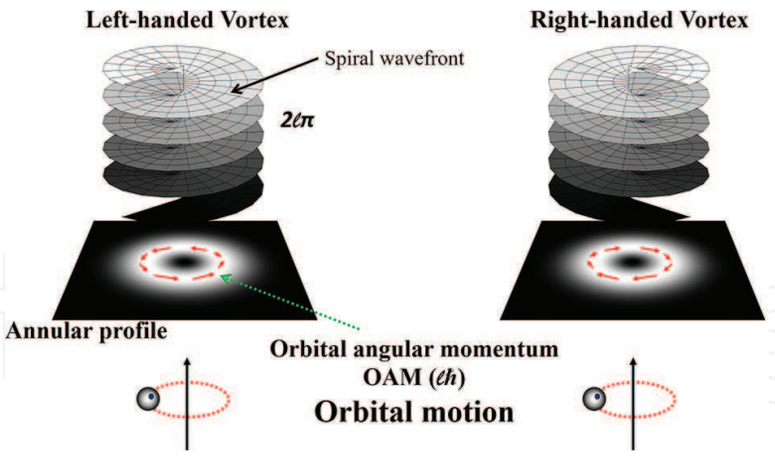

Figure 1. Optical vortex.

instance, they will enable advanced photonic devices [13], biomedical micro-electro-mechanical systems [14], ultrasensitive detector for chiral chemical composites [15] and plasmonic metasurfaces for chiral chemical reactions [16], etc.

2. Microneedle

2.1. Metal microneedle [17]

Metal microneedles, in particular, two-dimensional metal microneedle arrays should allow many applications, such as high-speed microscopic imaging [18], energy-saving field emission displays [19] and biomedical micro-electro-mechanical systems.

To date, several methods to fabricate metal microneedles have been proposed [20–22]; however, they are mostly based on a bottom-up technique including several chemical processes. Thus, their time- and cost-efficiencies are limited. Laser ablation, in which a target is broken down into its compositional elements, that is, ions and electrons, by the laser pulse illumination, has been widely studied for materials processing such as microdrilling [23], cutting [24] and scribing of metals [25], dielectric materials and semiconductors; however, it is ill-suited to collect compositional elements and create structured matters.

Laser ablation using optical vortex pulse (optical vortex laser ablation) [26], in which compositional elements created through laser ablation process receive orbital angular momentum from optical vortex pulse, enables us to fabricate structured materials. It allows us to form a metal microneedle with typically a 10 μm height and a <0.3 μm tip diameter merely by deposition of a few optical vortex pulses onto a metal, so as to fabricate two-dimensional metal microneedle arrays at high time- and cost-efficiencies [17].

A schematic diagram of an experimental setup for metal microneedle is shown in **Figure 2**. The circular polarization associated with a helical electric field also adds spin (s) angular momentum to the light [27]. The resulting circularly polarized optical vortex exhibits a total angular momentum (J) defined as the sum of the orbital (l) and spin (s) angular momenta [28]. The quarter-wave plate also suppressed the polarization dependence of the ablation efficiency.

http://dx.doi.org/10.5772/67073

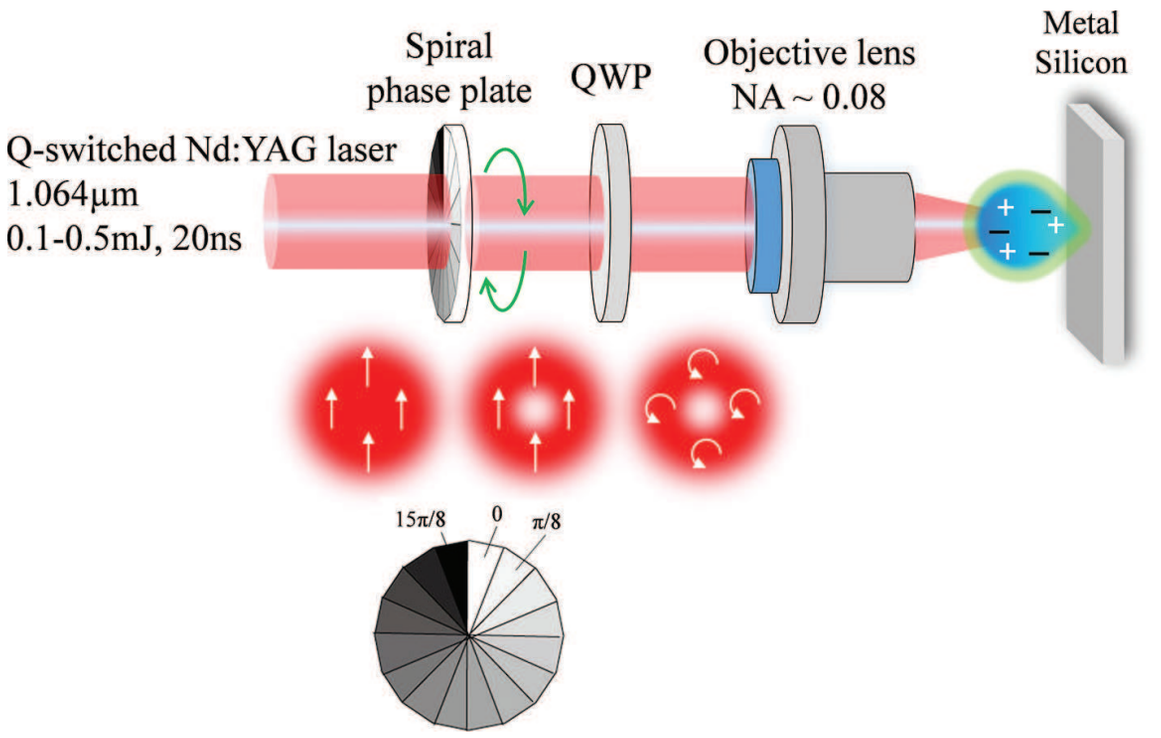

Figure 2. Schematic diagram of optical vortex laser ablation.

The target used was a polished tantalum plate with a 1-mm thickness. The pump laser used was a conventional Q-switched Nd:YAG laser with a wavelength of 1064 nm, a pulse duration of 30 ns and a Gaussian spatial form and its output was converted to the circularly polarized optical vortex by utilizing a spiral phase plate (SPP) [29], fabricated by electron beam etching, with azimuthal 2π phase and a quarter-wave plate. The optical vortex with $J = 2$ was focused to be ~130-μm annular spot onto the target output by an objective lens (M Plan Apo NIR, magnification factor 10, NA 0.26 from Mitutoyo Co.). The output energy on the sample surface was then fixed at 2 mJ. The ablated Ta plate was observed using a confocal laser-scanning microscope (Keyence VK-9700/VK9710GS) with a spatial resolution of 30 nm in both depth and transverse displacements. All experiments were performed at atmospheric pressure and room temperature.

Laser-scanning microscope images of processed Ta surfaces by optical vortex pumping are shown in **Figure 3**. After the single-shot deposition, a small bump with an approximately 4.4 μm height and 9.2 μm thickness appears at the center of the processed surface. When four optical vortex pulses were overlaid, the bump was shaped to be a needle with a height of ~10 μm and a tip diameter of less than 0.5 μm.

When $J = 0$ (the direction of the vortex is opposite to that of the circular polarization), in which the orbital and spin angular momenta work against with each other, the surface of Ta plate has no small bump and a lot of debris along the azimuthal direction around the outer circumference. Even when several pulses were overlaid onto the surface, only a small bump with an aspect ratio of <3 is structured.

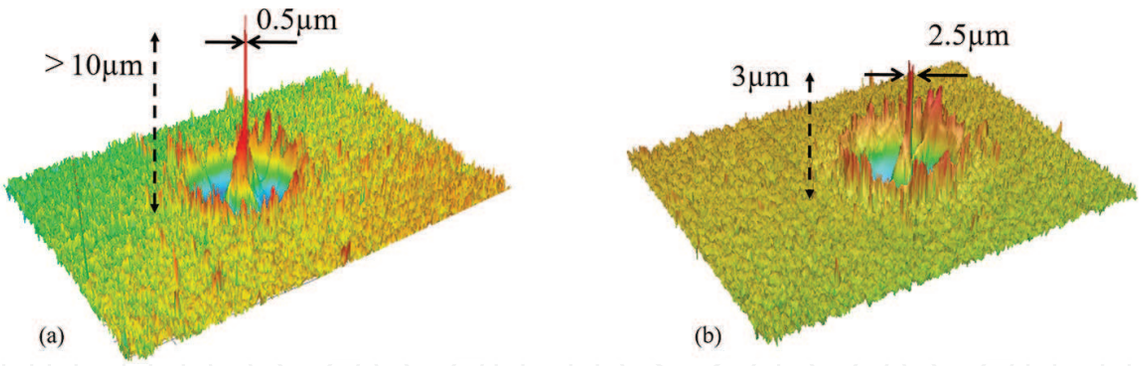

Figure 3. Metal microneedles fabricated by illumination of optical vortices with (a) $J = 2$ and (b) $J = 0$.

The following model will support the aforementioned experiments. The focused optical vortex forces the laser-induced melted or vaporized matters to revolve azimuthally along the annular intensity profile of the optical vortex. After that, the melted matter is confined in the dark core and accumulates at the center of the processed surface, resulting in a structured microneedle. We also successfully fabricated a two-dimensional and uniformly well-shaped 5 × 6 microneedle array with an average length and tip diameter of 11 and 0.5 μm by optical vortex laser ablation (**Figure 4**). Two optical vortex pulses are then overlaid on a target and after that, the target was translated.

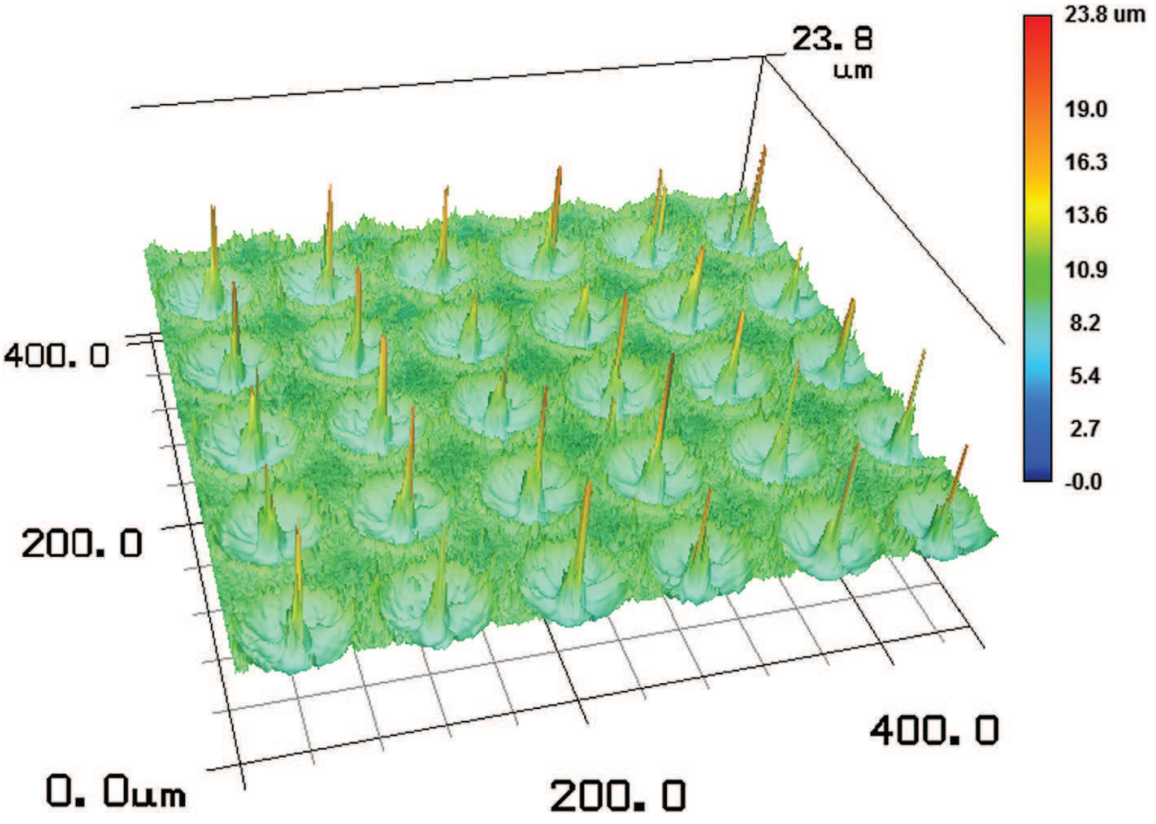

Figure 4. Two-dimensional microneedle array.

http://dx.doi.org/10.5772/67073

2.2. Silicon microneedle [30]

Monocrystalline silicon nano- or microstructures can improve significantly the performance of several photonic devices, such as photonic crystals [31], optical waveguides [32], photovoltaic devices [33], field emission arrays and metamaterials. Optical vortex laser ablation might provide us to fabricate silicon nanostructures at high cost- and time-efficiencies.

The experimental setup was almost identical with that in the metal microneedle fabrication. The pump laser used in this study was a picosecond Nd:YAG laser with a wavelength of 1064 nm, a pulse repetition rate of 10 Hz and a pulse duration of 20 ps and its output was converted to a circularly polarized optical vortex with a total angular momentum of 2. The optical vortex pulse was focused to be a 60-μm annular spot on the Si target by an object lens. A polished (100) monocrystalline silicon plate was used as the target. The ablated surface of the Si plate with a sputtered platinum coating was observed by a scanning electron microscope (JEOL, JSM-6010LA) with a spatial resolution of 8 nm at 3 kV. These experiments were also performed at atmospheric pressure and room temperature.

Picosecond optical vortex pulse with an energy of 0.6 mJ, which is sufficiently higher than the ablation threshold of ~0.03 mJ, was deposited on the target, so as to fabricate a debris-free needle with a height of 14 μm (the "length" defined as the length between the top and bottom ends of the needle was also measured to be 15 μm), a tip curvature of 160 nm and a thickness, defined as the full-width at 50% height of the needle, of approximately 2.9 μm (**Figure 5a**).

Worse heating effects arising from nanosecond pulse illumination (wavelength, 1064 nm; pulse energy, 0.6 mJ; pulse duration, 20 ns) suppress such needles formation, thereby yielding only a bump with a height of ~10μm (a length of ~12 μm) and a thickness of ~9.8 μm (>3 times that of the needle obtained by picosecond pulse illumination), even at the high-energy pumping (**Figure 5b**). These results indicate that the silicon needle formation requires picosecond pulse illumination with less heating effects.

Several overlaid picosecond vortex pulses enabled us to shape the needle with a height of ~40 μm. The experimental height, length and thickness of the needle as a function of the vortex pulse energy are shown in **Figure 6**.

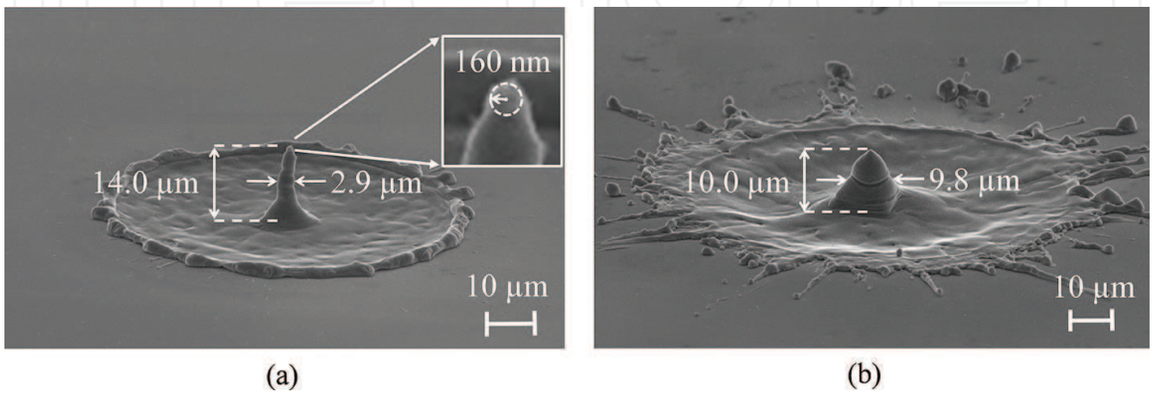

Figure 5. Monocrystalline silicon needles fabricated by (a) picosecond and (b) nanosecond optical vortex pulses.

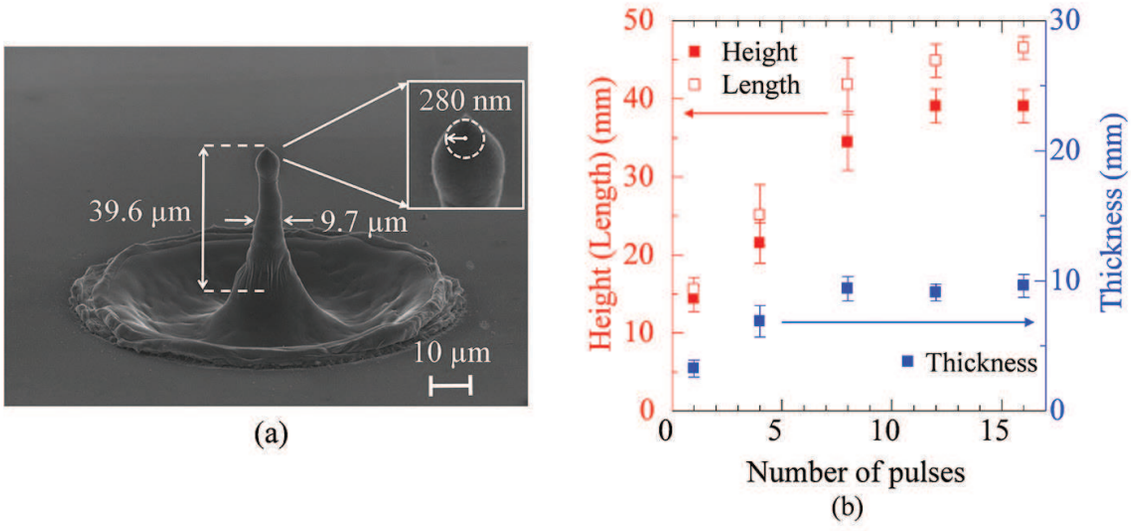

Figure 6. (a) Monocrystalline silicon needle by 10 overlaid vortex pulses and (b) height and thickness of the needle as a function of number of overlaid pulses.

The needle fabricated by picosecond vortex pulse irradiation exhibits the identical electron backscattering diffraction pattern to that of the silicon substrate with a lattice index of (1 0 0), although the needle had submicron-sized voids arising from thermal shock by illumination with optical vortex pulses (**Figure 7**). Namely, the monocrystalline needle was epitaxially grown on the silicon substrate.

In general, the silicon irradiated by ultrafast (femtosecond or picosecond) laser pulse was recrystallized mostly to form polycrystalline materials [34, 35]. How does the optical vortex illumination create such monocrystalline silicon structures?

The temporal dynamics of the silicon needle formation was investigated by utilizing an ultra-high-speed camera with a frame rate of 5×10^6 frame/s. Optical vortex pulse deposition provides the melted silicon optical radiation forces such as an optical angular momentum and a forward scattering force, $F_s(r)$, written as follows:

$$F_S \propto r^2 e^{-2r^2/\omega_0^2} \tag{1}$$

where $|u(r)|^2$ is the intensity profile of the optical vortex, r is the radial coordinate of the optical field and ω_0 is the beam waist of the vortex pulse on the Si substrate, respectively. The resulting radial gradient $\Delta F(r)$ of the forward scattering force around the dark core ($r < \omega_0$) is then given by

$$\Delta F_S \propto -2r e^{-2r^2/\omega_0^2} \cdot \left(1 - 2\frac{r^2}{\omega_0^2}\right) \approx -2r. \tag{2}$$

The radial gradient $\Delta F(r)$ acts as a restoring force to collect the melted silicon within the dark core of the optical vortex. Also, the vaporization-induced recoil pressure [36] directs the melted silicon to the dark core. After the vortex pulse is gone (the recoil pressure is also gone), the melted silicon further transports toward the dark core by thermal diffusion effects. An

http://dx.doi.org/10.5772/67073

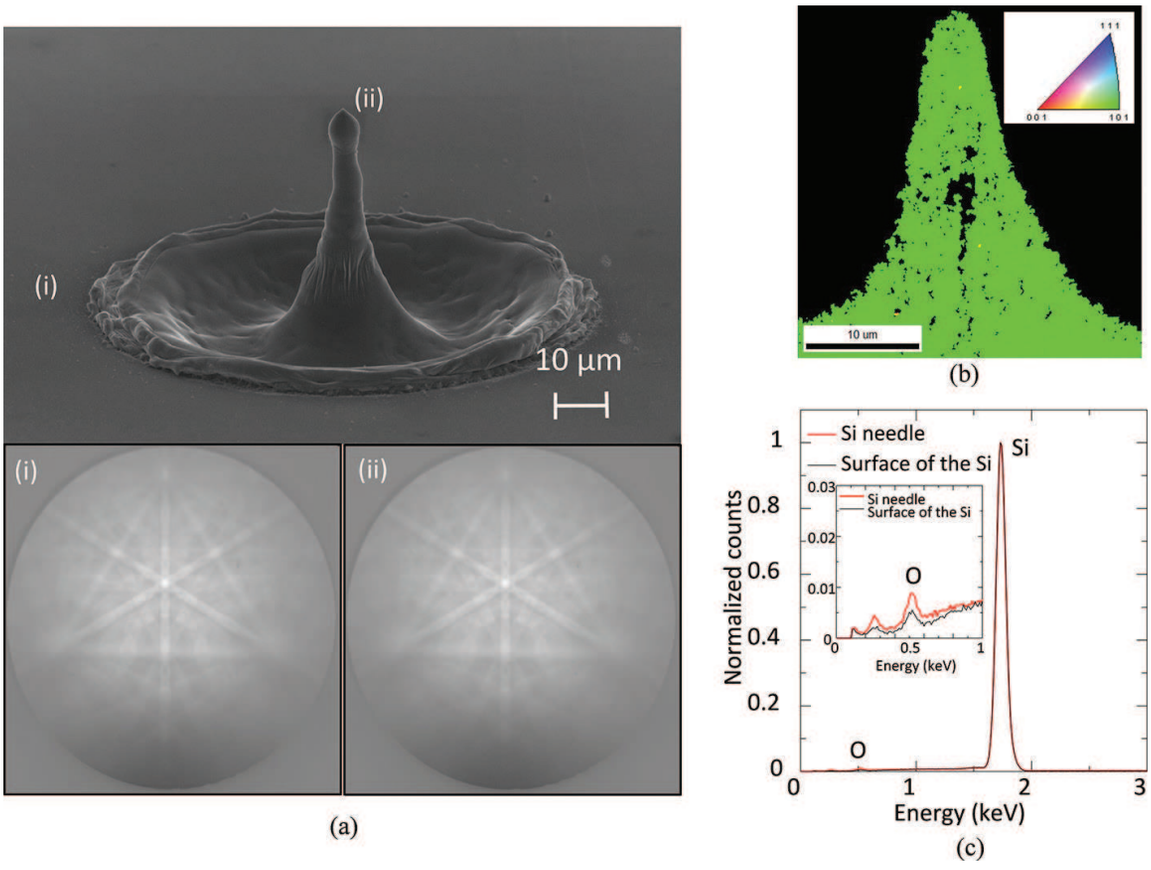

Figure 7. (a) Electron backscattering pattern of the silicon needle, (b) lattice index of the silicon needle and (c) energy dispersive X-ray spectrum of the silicon needle.

additional 200–600 ns later, the silicon is supercooled to recrystallize at the core (**Figure 8a**). A capillary wave [36] induced by the optical vortex illumination also ejects superfluous silicon droplets with a radius a given by the following formula,

$$a = \frac{3\pi\sigma}{4\rho v^2\sqrt{1-M^2}} \tag{3}$$

where σ is the surface tension coefficient (770 mN/m), v is the velocity of the silicon droplet (~50 m/s; the velocity was estimated from **Figure 8a**) and M is the Mach number (~0.3), respectively. The estimated a (~1.3 μm) is consistent with experimental one (~2.0 μm). Such slow solid-liquid hydrodynamics at a microsecond time scale enables us to establish the monocrystalline silicon needle.

Also, the silicon was pumped by a circularly polarized annular beam with the pulse energy of 0.8 mJ (without any orbital angular momentum) produced by a damaged mirror. The silicon cone-shaped structure with a height of ~9.0 μm and a thickness of ~3.6 μm then was formed. The silicon droplets flied away with a wide divergence angle θ (>6°) from the silicon substrate, so as to impact efficient accumulation of the silicon on the substrate (**Figure 8b**). We conclude that such straight flight straight flight of silicon droplets with spinning motion is induced by the optical vortices to establish the silicon needle.

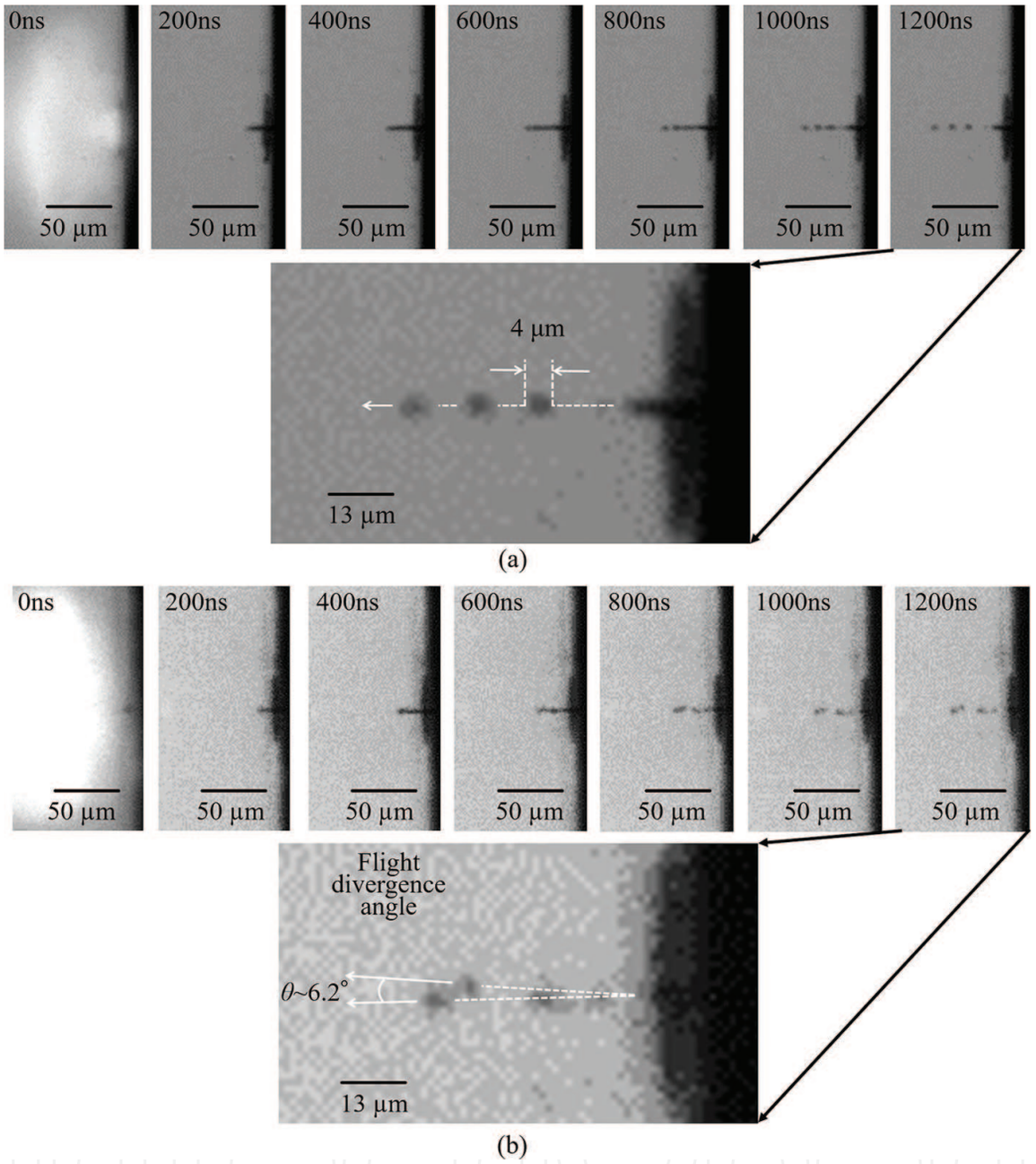

Figure 8. Temporal evolutions of silicon needle formation pumped by (a) optical vortex pulse and (b) annular beam without orbital angular momentum.

The spinning motion of the droplets cannot be directly observed, because of a relatively low spatial resolution (~1.2 μm) of the high-speed camera and it should be further investigated by utilizing nanosecond pump–probe analysis with high spatial and temporal resolutions [37].

Also, note that the spin–orbital angular momentum coupling effect is negligible in the present experiments based on optical vortex pumping with a low numerical aperture and a short pulse duration. The fabrication efficiency of the needles is almost 100%, though the individual needles to exhibit an individual length and height with a relatively large standard error of 3–4 μm.

3. Chiral structures

3.1. Chiral metal nanoneedle [38, 39]

Chiral metal nanoneedles will explore potentially various material sciences, for instance, selective assignment of the chirality and optical activity of molecules and chemical composites on a nanoscale and asymmetric chemical synthesis on plasmonic metasurfaces. However, no technique for twisting metal to form chiral metal nanoneedles has been established yet. Laser material processing has not been used to produce chiral metal nanoneedles, either.

Optical vortex with a helical wave front carries a handedness determined by the sign of the orbital angular momentum. If optical vortices can transfer their handedness to the melted metal through laser ablation processes, they will twist metal to form chiral metal nanoneedles.

Schematic diagram of experimental setup is almost identical with that as shown in **Figure 2**. A circularly polarized nanosecond optical vortex pulse (wavelength 1 μm, pulse width 30 ns, total angular momentum 2) was focused to be an annular spatial form with a diameter of <65 μm onto a metal. Four vortex pulses then were overlaid. The pulse energy was ~0.3 mJ, corresponding to <1/6 that used in Section 2. The handedness of the optical vortex pulse was reversed by inverting the SPP and QWP.

A needle with a tip curvature of <72 nm and a height of <10 μm, respectively, was formed at the center of the ablated zone with a smooth outline (**Figure 9a**) and its conical surface was also twisted azimuthally in the clockwise direction (**Figure 9b**). At higher energy pumping, the chiral nanoneedle formation was inhibited. When the handedness of the optical vortex (total angular momentum 2) was reversed, a needle was twisted azimuthally in the counterclockwise direction (**Figure 9c** and **d**). These results, in which the handedness of the optical vortex can determine the twisting direction, for example, chirality of the nanoneedle, evidence that the metal melt by optical vortex illumination is forced to revolve azimuthally around the dark core by orbital angular momentum transfer effects.

The tip curvature of the twisted nanoneedle was further found to be inversely proportional to NA of the focusing optics (vortex pulse fluence was fixed to <9 J/cm^2) and the minimum value was measured to be 36 nm, which is <1/25 of the optical vortex wavelength (1064 nm) (**Figure 10**).

The electric resistance of the nanoneedle was measured to be <0.05 Ω by using two 50-μm-diameter tungsten probes. This value was identical to that of the substrate. Energy-dispersive X-ray (EDX) spectrum of the nanoneedle was also almost identical to that of the substrate, evidencing that the nanoneedle is perfectly metallic (**Figure 11**).

To make clear whether the wave front or polarization helicity primarily contributes to chiral nanoneedle fabrication or whether both helicities have similar contributions to chiral nanoneedle formation, the structures of chiral nanoneedles were further studied by using optical vortices with various values of the angular momenta J, l and s. The numerical aperture of the objective lens and the optical vortex pulse energy were then tuned in the range of 0.04–0.15 and 0.2–0.8 mJ, respectively, so as to maintain a constant beam waist and a constant fluence.

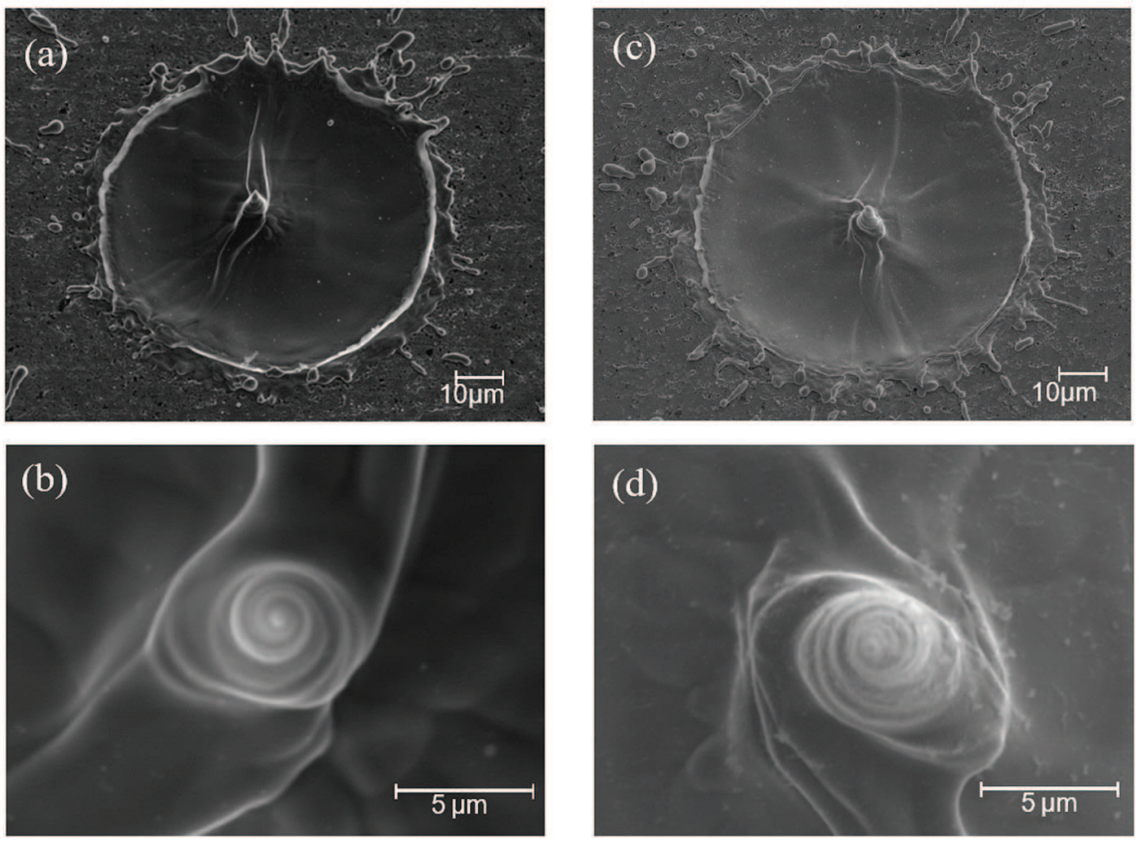

Figure 9. Chiral metal nanoneedles. (a) and (b) Left-handed needle, (c) and (d) right-handed needle.

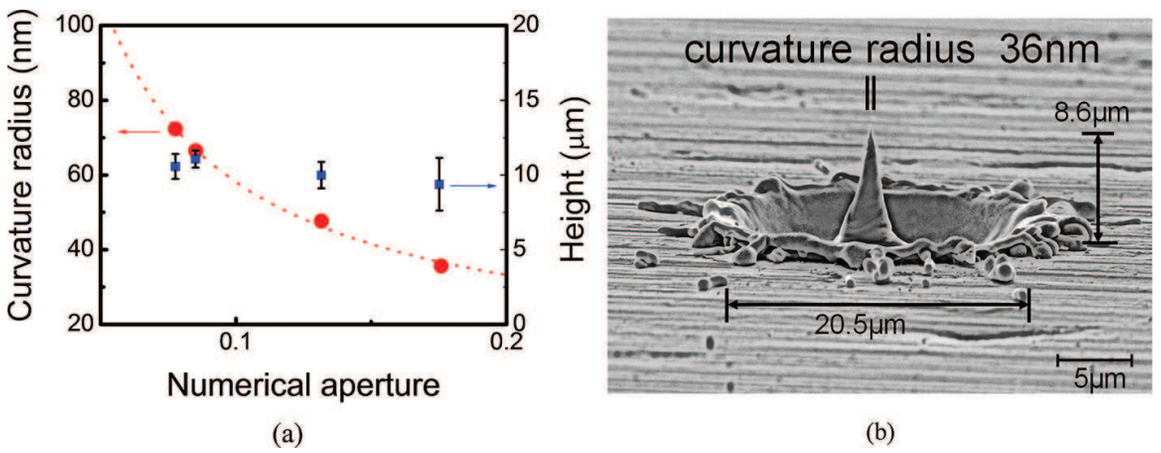

Figure 10. (a) Tip curvature of the nanoneedle as a function of NA and (b) nanoneedle with a tip curvature of 36 nm.

The chirality of the nanoneedles is determined only by the handedness of orbital angular momentum l (the handedness of spin angular momentum s does not matter). The spiral density of the nanoneedle (defined as the number of turns divided by the length of the nanoneedle) was determined by the magnitude of J rather than l and it also increased as increasing

http://dx.doi.org/10.5772/67073

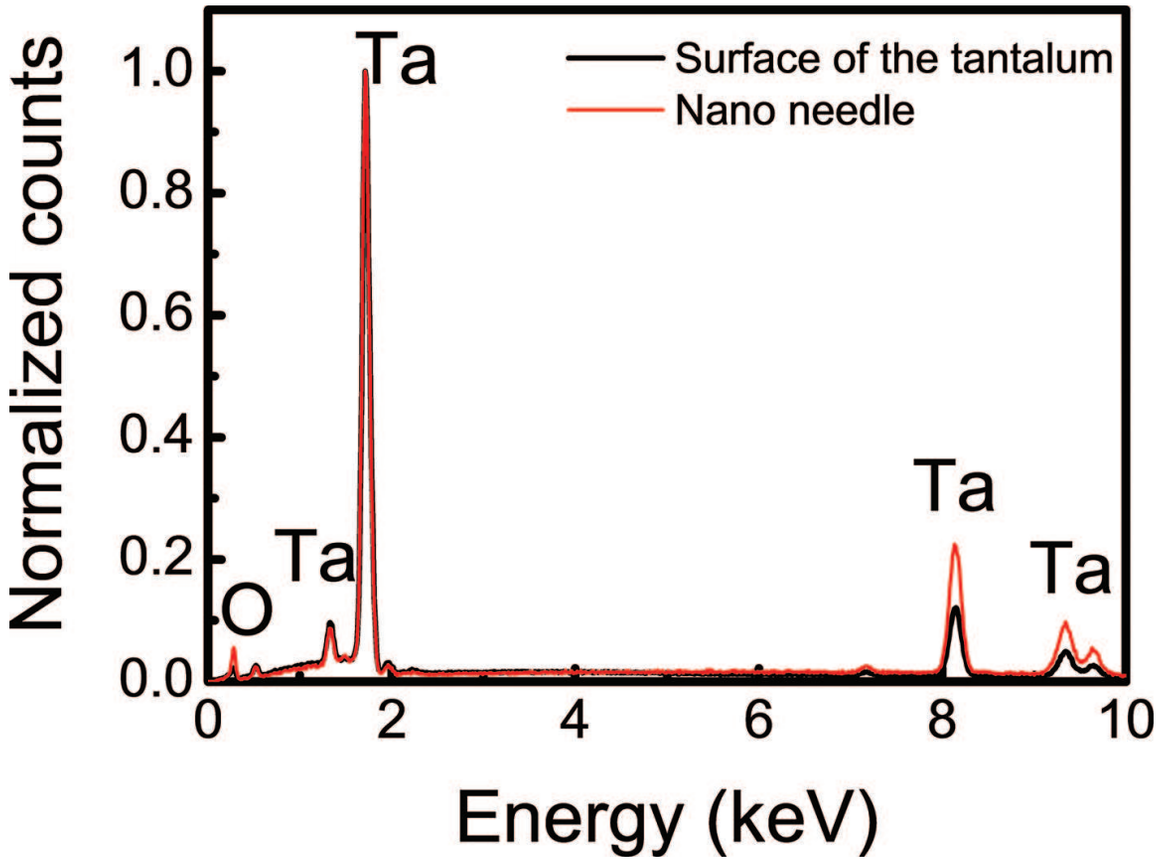

Figure 11. Energy dispersive X-ray spectrum of the 36-nm chiral metal nanoneedle.

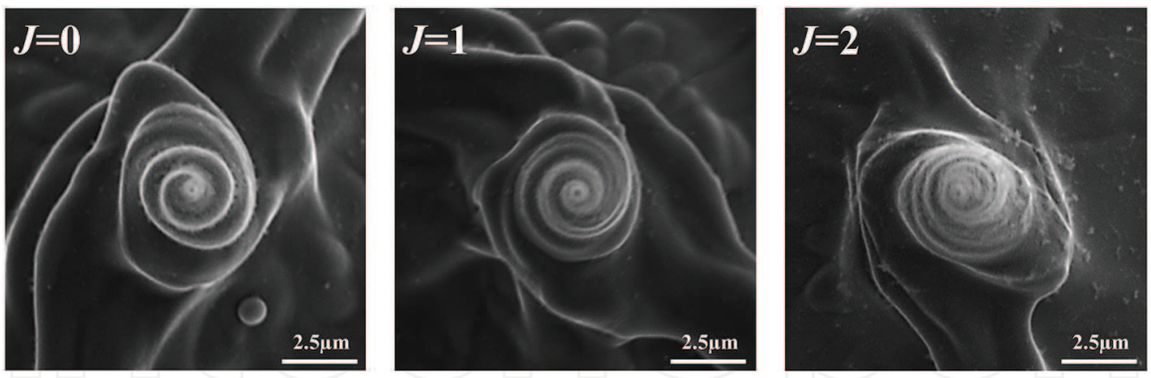

Figure 12. Chiral nanoneedles at total angular momenta J of 0, 1 and 2.

J (**Figure 12**). Namely, it is found that nanoneedles created by linearly polarized second-order (l = 2, s = 0) and circularly polarized first-order (l = 1, s = 1) optical vortices exhibit the same chirality and spiral density (**Figure 13**).

3.2. Other chiral structures [40]

Chiral monocrystalline silicon nanostructures are difficult to fabricate even by utilizing advanced chemical technologies [41, 42].

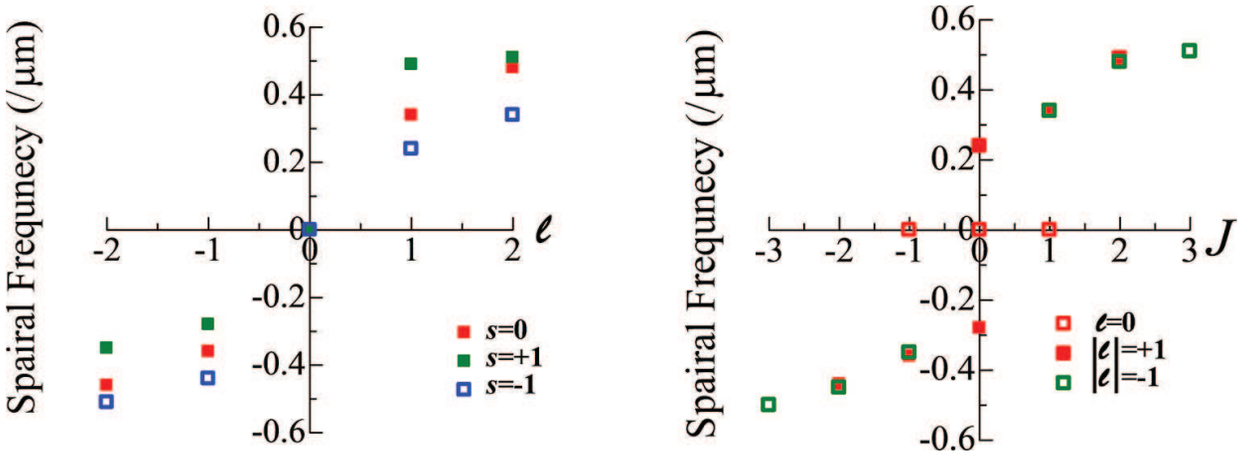

Figure 13. Spiral frequency of chiral metal nanoneedle at various *J*, *l* and *s*.

The target used was a polished (1 0 0) monocrystalline silicon plate. The circularly polarized nanosecond optical vortex pulse (total angular momentum 2) was focused to be a φ25-μm annular spot onto a silicon. With this system, the experimental ablation threshold of the silicon was measured to be 0.02 mJ.

At a pulse energy of 0.1 mJ, a silicon cone with a spiral conical surface (chiral silicon cone) was fabricated and its tip curvature and height were measured to be 110 nm and 1.0 μm, respectively (**Figure 14**).

The length of the chiral silicon cone was also measured to be 4.8 μm. The chirality of the silicon cone was also reversed by inverting the handedness of the optical vortex pulse.

Also, note that the silicon cone had the lattice index of (1 0 0) and its electron diffraction pattern and Raman spectrum were fully identical with those for the silicon substrate.

Even a copper, which has been widely investigated as a plasmonic metal, was twisted by optical vortex illumination, so as to form chiral needles (**Figure 15**).

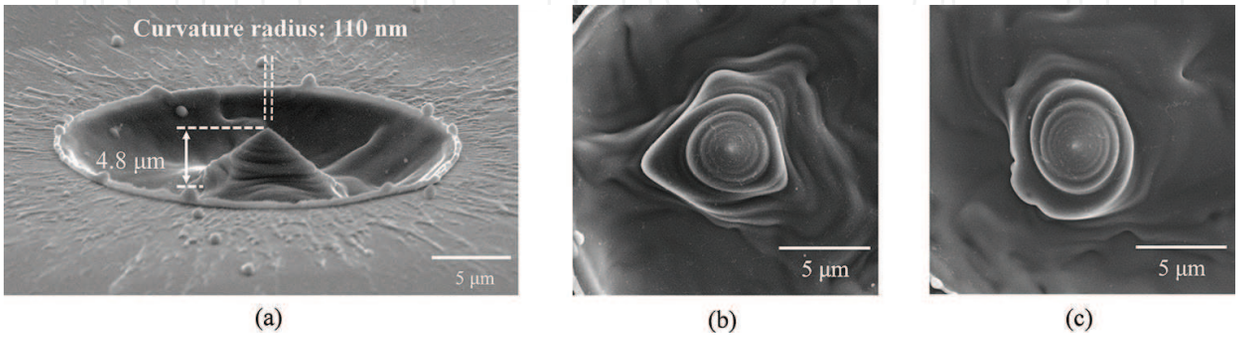

Figure 14. (a) Chiral silicon cone, (b) right-handed cone and (c) left-handed cone.

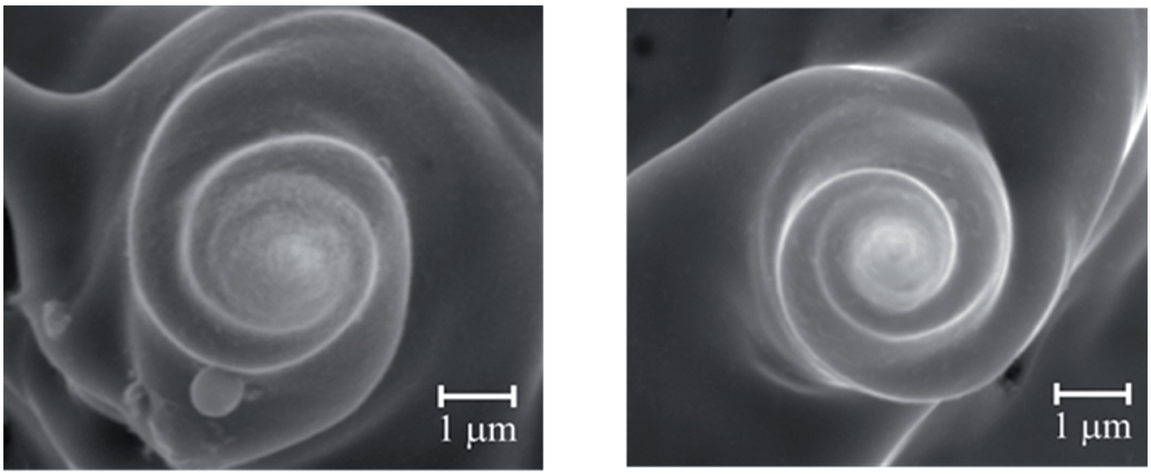

Figure 15. Left-handed and right-handed copper needles.

4. Surface relief

4.1. Chiral surface relief formation [43]

Surface relief formation has been established on azo-polymer films through mass transport owing to a driving force based on an optical gradient force, anisotropic photo-fluidity and cis-trans photoisomerization [44, 45]. Such surface relief provides many photonic devices, for instance, holographic memories [46], holographic waveguides [47] and photonic circuits.

In general, the mass transport driving force arises from the spatially inhomogenous intensity of the structured illumination, so as to direct the azo-polymer from a bright fringe toward a dark fringe along the polarization direction of the light. Thus, a spiral surface relief formation even by using circularly polarization is mostly inhibited.

Ambrosio et al. demonstrated the formation of spiral surface relief (termed "spiral relief" in their work), in which tightly focused higher-order optical vortices with a high numerical aperture (NA ~1.3) objective lens create a spiral surface relief with a shallow depth (10–20 nm) through azimuthal mass transport owing to interference between longitudinal and transverse optical fields [48].

Recently, we first demonstrated the formation of a single-arm chiral surface relief with a deep modulation depth of over 1 μm by using a lower-order optical vortex together with the spin angular momentum associated with the circular polarization.

A ~4 μm-thick-spin-coated azo-polymer (poly-orange tom-1, POT) film [49] used had absorption band in the wavelength range of 300–550 nm; thus, it exhibits a photo-isomerization behavior by green laser irradiation (**Figure 16**). A continuous-wave frequency-doubled

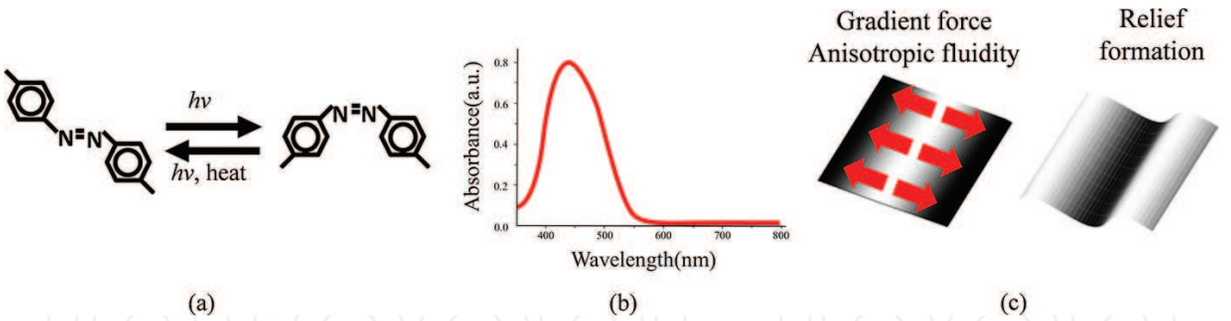

Figure 16. (a) Photoisomerization of azo-polymer, (b) absorption of poly orange-tom 1 and (c) mass transport on azo-polymer film to form surface relief.

Nd:YVO_4 laser output (a wavelength of 532 nm) was converted to be a circularly polarized first-order optical vortex by employing a computer-generated hologram displayed on a spatial light modulator (Hamamatsu photonics, X10468-03) and a quarter-wave plate. The sign of the orbital angular momentum was then made the same (or opposite) to that of the spin angular momentum, resulting in the total angular momentum *J* of 2 or 0. The optical vortex beam with a power of ~300 μW was focused to an annular spot with a diameter of 4 μm on the azo-polymer film by an objective lens with NA ~0.45, corresponding to a focused spot intensity of ~2.5 kW/cm^2. An exposure time on the film was fixed to be 8 s. All experiments were performed at room temperature and in the atmosphere.

In the case of a linearly polarized optical vortex, the mass transport occurs along the polarization direction to collect azo-polymer toward the dark core, so as to establish a cat-shaped (non-spiral) surface relief (**Figure 17a**). Loosely focusing in our experiments impacts to produce transverse optical field, thereby preventing the spiral surface relief.

A circularly polarized optical vortex with positive orbital and spin angular momenta forces the orbital motion of the azo-polymer in a clockwise direction to complete a single-arm spiral structure. The resulting chiral surface relief then had a height of ~1 μm and a diameter of ~5 μm, respectively (**Figure 17b**). In contrast, a circularly polarized optical vortex beam with negative spin angular momentum inhibited the spiral surface relief formation to establish only non-spiral bump relief (**Figure 17c**).

Only circularly polarized optical vortex with positive (or negative) orbital and positive (or negative) spin angular momenta can produce such clockwise (or counter-clockwise) spiral surface relief on the azo-polymer film for all topological charges in a range of 1 3. The experimental data are summarized in **Figure 18**.

In general, mass transport arising from the photo-isomerization occurs at a temperature below the glass transition temperature of the polymer, meaning that the polymer volume before and after the relief formation should be preserved [50]. In fact, the spiral surface relief can be easily erased by the spatially uniform green laser illumination (0.36 W/cm^2), indicating that photo-isomerization but rather heat-induced effects (melting, expansions, ablation, etc.) contributes predominantly to the spiral surface relief formation (**Figure 19**).

http://dx.doi.org/10.5772/67073

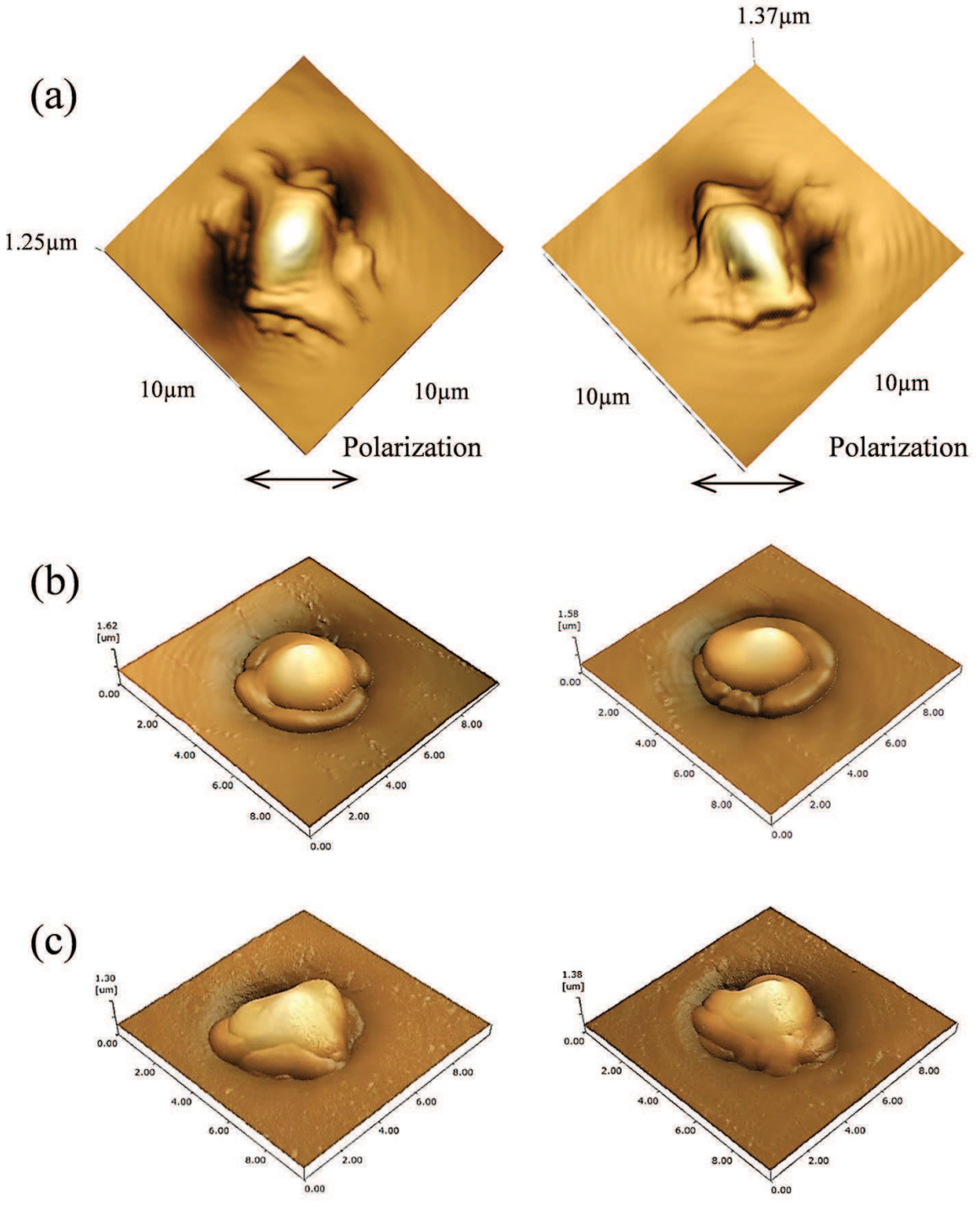

Figure 17. Surface reliefs formed in azo-polymer film by illumination of (a) linearly polarized optical vortex, (b) circularly polarized optical vortex with total angular momentum *J* of 2, and (c) circularly polarized optical vortex with total angular momentum *J* of 0.

4.2. Theoretical discussion [51]

Why can organic azo-polymers be deformed to create a chiral surface relief by circularly polarized optical vortices with positive (or negative) orbital and positive (or negative) spin angular momenta?

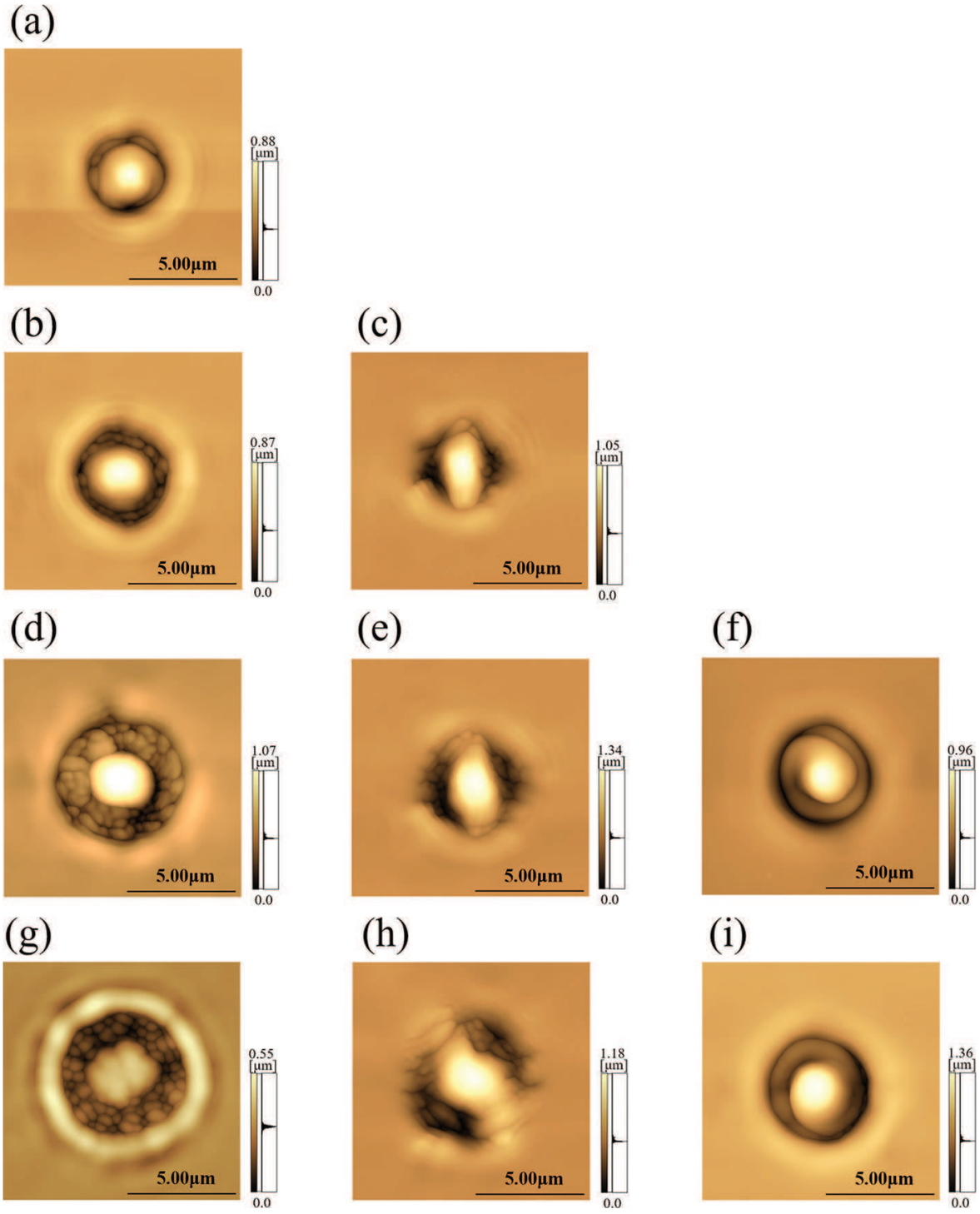

Figure 18. Surface reliefs formed in an azo-polymer thin film by irradiation with optical vortices with spin and orbital angular momenta of (a) $J = 0$ ($l = 1$, $s = -1$), (b) $J = 1$ ($l = 2$, $s = -1$), (c) $J = 1$ ($l = 1$, $s = 0$), (d) $J = 2$ ($l = 3$, $s = -1$), (e) $J = 2$ ($l = 2$, $s = 0$), (f) $J = 2$ ($l = 1$, $s = 1$), (g) $J = 3$ ($l = 4$, $s = -1$), (h) $J = 3$ ($l = 3$, $s = 0$), and (i) $J = 3$ ($l = 2$, $s = 1$).

Conventional optical manipulation, in which particles play a role as electric dipoles with optically induced surface charges at the interface between themselves and a solution, has been theoretically well established [52, 53]. However, there were few theoretical works concerning the formation of spiral structures in isotropic and homogeneous materials using the optical radiation force, in which the wavefront-sensitive light-induced mass transport occurs.

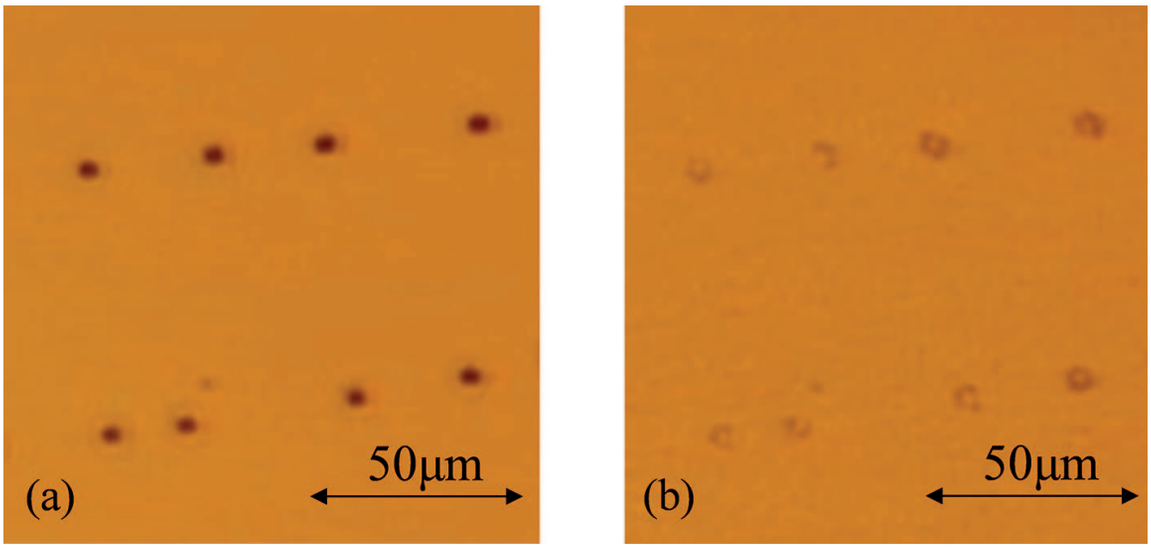

Figure 19. (a) Microscope image of surface relief before uniform green laser irradiation and (b) microscope image of surface relief after uniform green laser irradiation.

A few researchers have proposed theoretical models for such light-induced wavefront-sensitive mass transport in the azo-polymer, in which the azo-molecule is considered to be a microscopic dipole; however, their models based on a finite difference time-domain method are difficult to understand directly how the azo-polymer homogeneous materials deform by optical vortex illumination and how the spin and orbital angular momenta contribute to wavefront-sensitive structures formation? [54–56]

An analytical formula for the optical vortex induced optical radiation force in an isotropic and homogeneous material is proposed, so as to directly understand how the homogenous materials deform by the irradiation of optical vortices with arbitrary orbital and spin angular momenta.

The optically induced polarization charge density on an isotropic and homogeneous material surface is zero; thus, the time-averaged optical radiation force F arising from optically induced electric polarization is expressed by

$$F = \langle -i\omega\,\varepsilon_0\,\chi E \times B \rangle = \frac{\omega\,\varepsilon_0}{2}\left[\chi_r\,\mathrm{Im}(E \times B^*) + \chi_i\,\mathrm{Re}(E \times B^*)\right] \tag{4}$$

where **E** is the electric field vector, **B** is the magnetic flux density vector, ε_0 is the dielectric constant in a vacuum, ω is the angular frequency of the optical field and χ (= $\chi_r + i\chi_i$) is the macroscopic complex electric susceptibility, respectively. The angle brackets < > then denote the time average.

Assuming a paraxial approximation, in which the continuous-wave optical vortex beam is loosely focused and it propagates along the z-axis without diffraction in the material, the scholar electric field, $E(r, \phi, z)$, of the right-handed optical vortex with a positive topological charge in cylindrical coordinates is given by,

$$E(r, \phi, z) = A_\ell(r)\, e^{ikz}\, e^{i\ell\phi}\, e^{-i\omega t} \tag{5}$$

where $A_l(r)$ is the axisymmetric amplitude and k is the wave number.

The resulting optical radiation force **F** can be expressed as follows:

$$F(r,\phi,z) = \frac{\varepsilon_0 \chi_r}{4}\left\{\frac{\sqrt{1-s^2}}{2}\frac{\partial A_\ell^2}{\partial r}\left(-\cos\phi\cdot e_x+\sin\phi\cdot e_y\right)+\left(\frac{1}{2}\frac{\partial A_\ell^2}{\partial r}-\ell s\frac{A_\ell^2}{r}\right)e_r\right\}$$
$$+\frac{\varepsilon_0 \chi_i}{4}\left\{\ell\frac{\sqrt{1-s^2}}{2}\frac{A_\ell^2}{r}\left(\sin\phi\cdot e_x+\cos\phi\cdot e_y\right)+\left(\ell\frac{A_\ell^2}{r}-\frac{s}{2}\frac{\partial A_\ell^2}{\partial r}\right)e_\phi+2k A_\ell^2 e_z\right\} \quad (6)$$

where $\mathbf{e}_r$, $\mathbf{e}_f$ and $\mathbf{e}_z$ are the unit vectors along the r, ϕ and z-axes, respectively; $\mathbf{e}_x$ and $\mathbf{e}_y$ are also unit vectors for the polarization state in a Cartesian coordinate system.

The optical radiation force, given by the first and second terms in Eq. (6), is proportional to the gradient of the optical intensity along the polarization direction and it plays a role as the mass transport driving force. The radial optical radiation force, expressed as the third and fourth terms in Eq. (6), acts as a restoring (or repulsive) force to direct the materials toward (or outwards from) the dark inner core of the optical vortex with a mode field radius of $x_{0.}$

The axisymmetric amplitude $A_l(r)$ is given as

$$A_\ell(r) = \frac{A_0}{\sqrt{\ell!}}\left(\sqrt{2}\,\frac{r}{\omega_0}\right)^{|\ell|} e^{-\frac{r^2}{\omega_0^2}}. \quad (7)$$

Also, note that the radial optical radiation force is proportional to the real part χ_r of the polarization susceptibility. The optical absorption force (fifth and sixth terms), which is proportional to the imaginary part χ_i of the electric susceptibility, also gives the torque to the materials. The optical absorption force given by the seventh and eighth also induces the orbital motion of materials around the dark core. The forward scattering force given by the last term also serves as a restorative force to confine the materials to the inner dark core, thereby yielding the radial force proportional to the gradient of the forward scattering force.

A linearly x-polarized optical vortex without spin angular momentum ($s = 0$) exhibits the optical radiation force **F** given by,

$$F(r,\phi,z) = \frac{\varepsilon_0}{2}\left(A_\ell^2\right)\cdot\left[\left\{\left(\frac{\ell}{r}-\frac{2r}{\omega_0^2}\right)\chi_r\sin\phi-\frac{\ell}{r}\chi_i\cos\phi\right\}e_y+k\chi_i e_z\right]. \quad (8)$$

The optical radiation force provides mostly the clockwise torque to the materials along the y direction (along the vertical direction to the polarization) and thereby, it prevents chiral structures formation. The complex electric susceptibility of the material was then assumed to be $2 + 2i$, corresponding to that of the azo-polymer. The gradient of forward scattering force will also drive the materials toward the dark core of the optical vortex, resulting in the mass transport along the x direction (along the direction of polarization).

The circularly polarized optical vortex ($s = \pm 0$) produces the optical radiation force written as follows:

$$F(r,\phi,z) = \frac{\varepsilon_0 \chi_r}{2}\cdot\left(|\ell|-\ell s-\frac{2r^2}{\omega_0^2}\right)\left(\frac{A_\ell^2}{r}\right)e_r+\frac{\varepsilon_0 \chi_i}{2}\cdot\left\{\left(\ell-|\ell|s+s\frac{2r^2}{\omega_0^2}\right)\left(\frac{A_\ell^2}{r}\right)e_\phi+2k A_\ell^2 e_z\right\}. \quad (9)$$

http://dx.doi.org/10.5772/67073

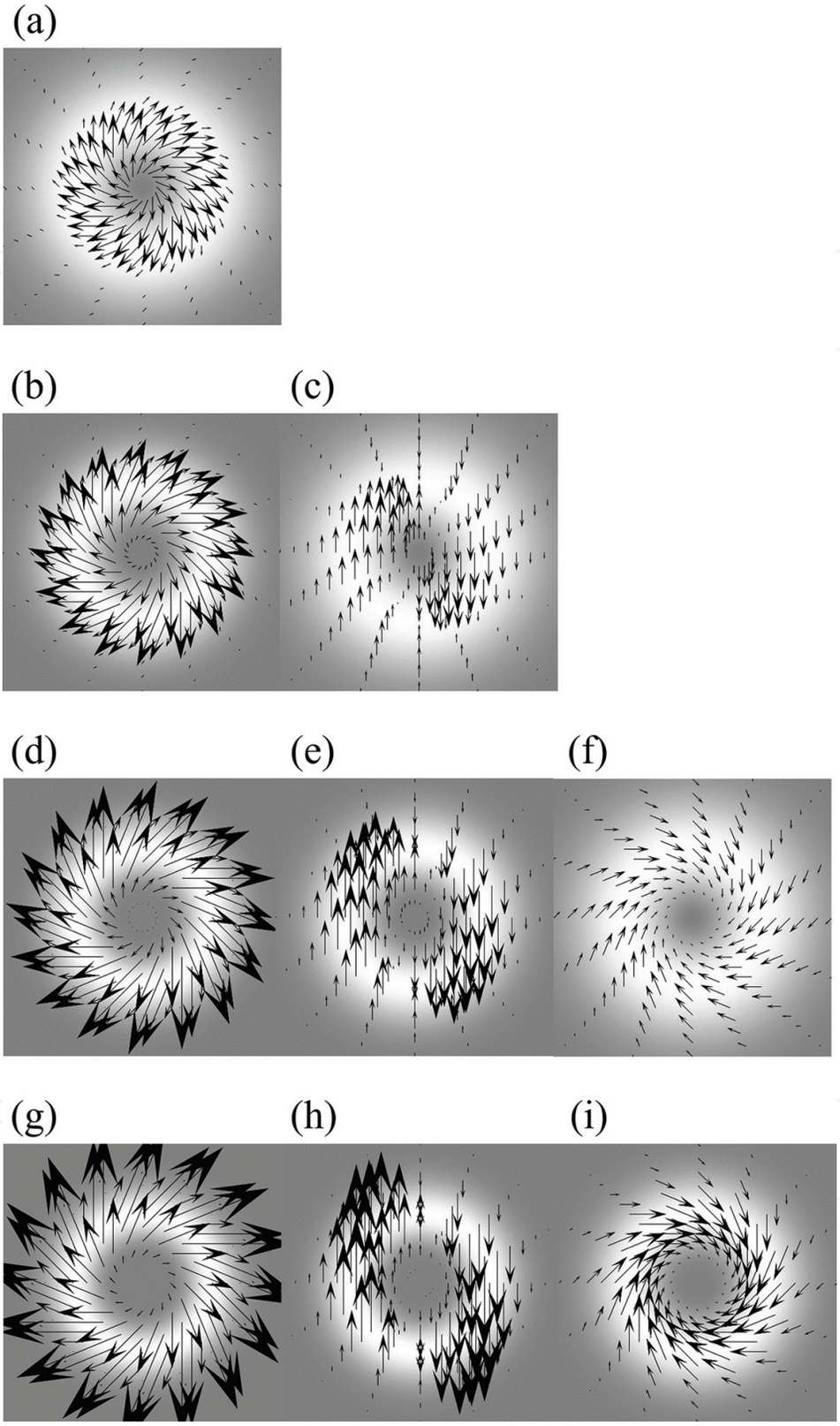

Figure 20. Spatial distributions of the radial and azimuthal optical radiation forces produced by optical vortices with total angular momenta of (a) $J = 0$ ($l = 1$, $s = -1$), (b) $J = 1$ ($l = 2$, $s = -1$), (c) $J = 1$ ($l = 1$, $s = 0$), (d) $J = 2$ ($l = 3$, $s = -1$), (e) $J = 2$ ($l = 2$, $s = 0$), (f) $J = 2$ ($l = 1$, $s = 1$), (g) $J = 3$ ($l = 4$, $s = -1$), (h) $J = 3$ ($l = 3$, $s = 0$), and (i) $J = 3$ ($l = 2$, $s = 1$). The optical field of the vortex, shown in white, underlies the optical radiation forces.

When the product of l and s is positive, the radial optical radiation force acts as a restoring force for the materials toward the dark core and the azimuthal optical absorption force drives the orbital motion of the materials around the dark core. The forward scattering force also plays a role as the restoring force to confine the materials inside the dark core, thereby establishing a chiral structure.

In the case of the negative product of l and s, the optical vortex provides the repulsive radial optical radiation force, which competes with the effective radial force produced by the forward scattering force, so as to prevent the efficient confinement of the materials in the dark core. Furthermore, the radial radiation force and azimuthal absorption force are reversed outside the dark core. The resulting non-twisted orbital motion of the materials will occur, thereby yielding non-chiral structures (**Figure 20**).

These results, in which only optical vortices with a positive product of orbital and spin angular momenta (constructive spin-orbital coupling) enable the formation of chiral structures, can support well the experiments of the chiral surface relief formation in the azo-polymer film. The degeneracy among optical vortices with the same total angular momentum J is then resolved.

As mention in Section 3, the pulsed optical vortices illumination forms spiral metal structures, in which the melted metal is collected in the dark core after the vortex pulse has gone. Only an optical absorption force $\mathbf{F}^{l,s}$ will then act as the mass transport driving force through the laser ablation process. The resulting general relationship given by

$$F^{\ell-1,1} = F^{\ell,0} \quad \ell \geq 2 \tag{10}$$

is established.

Two optical vortices with the same total angular momentum J should provide the same azimuthal optical radiation force and they are degenerate. This theoretical analysis can also support well the experimental results obtained previously in the metal with pulsed optical vortices illumination.

5. Conclusion

The optical vortex carries an annular intensity profile and an orbital angular momentum owing to a helical wave front. We discovered, for the first time, that the optical vortex with orbital angular momentum enables us to twist a melted metal, silicon and a photo-isomerized polymer to establish monocrystalline achiral or chiral structures (i.e., microneedles, microspheres, chiral nanostructures and chiral surface relief). The chirality of the structured materials is determined selectively by the handedness of the optical vortex. A spin angular momentum arising from to a helical electric field of the circular polarization then accelerates (or decelerates) the chiral materials formation. Two-dimensional chiral nanostructures array can be easily fabricated merely by translating the target and then irradiating the optical vortex onto the target.

We also found that chiral surface relief formation in the azo-polymers requires the irradiation with continuous-wave optical vortices with a positive product of orbital and spin angular momenta (constructive spin-orbital angular momentum coupling); therefore, the degeneracy among the optical vortices with the same total angular momentum is resolved.

In contrast, spiral metal structures formation by the pulsed optical vortices illumination, the melted metal receives only an optical absorption force as the mass transport driving force through the laser ablation process. Thus, optical vortices with the same total angular momentum J are degenerate and they create the same chiral structures.

Such chiral nanostructures will open potentially the door to develop various advanced material sciences and technologies, such as selective identification of chiral chemical composites, enhancement of chiral chemical reactions, plasmonic metasurfaces, nanoimaging systems, energy-saving displays and biomedical nanoelectromechanical systems.

Acknowledgements

The authors acknowledge a JST-CREST Grant and a JSPS KAKENHI Grant Number JP 16H06507 in Scientific Research on Innovative Areas "Nano-Material Optical-Manipulation".

Author details

Takashige Omatsu[1]*, Katsuhiko Miyamoto[2] and Ryuji Morita[3]

*Address all correspondence to: omatsu@faculty.chiba-u.jp

1 Graduate School of Advanced Integration Science, Chiba University, Chiba, Japan

2 Molecular Chirality Research Center, Chiba University, Chiba, Japan

3 Graduate School of Engineering, Hokkaido University, Sapporo, Japan

References

[1] L. Allen, M. W. Beijersbergen, R. J. C. Spreeuw and J. P. Woerdman, "Orbital angular momentum of light and the transformation of Laguerre–Gaussian laser modes," Phys. Rev. A, **45**(11), 8185–8189 (1992).

[2] M. Padgett, J. Courtial and L. Allen, "Light's orbital angular momentum," Phys. Today, **57**(5), 35–40 (2004).

[3] M. J. Padgett, F. M. Miatto, M. P. J. Lavery, A. Zeilinger and R. W. Boyd, "Divergence of an orbital-angularmomentum-carrying beam upon propagation," New J. Phys., **17**(2), 023011 (2015).

[4] T. Kuga, Y. Torii, N. Shiokawa, T. Hirano, Y. Shimizu and H. Sasada, "Novel optical trap of atoms with a doughnut beam," Phys. Rev. Lett., **78**(25), 4713–4716 (1997).

[5] M. Padgett and R. Bowman, "Tweezers with a twist," Nat. Photonics, **5**, 343–348 (2011).

[6] D. G. Grier, "A revolution in optical manipulation," Nature **424**, 810–816 (2003).

[7] J. Wang, J. Yuan Yang, I. M. Fazal, N. Ahmed, Y. Yan, H. Huang, Y. X. Ren, Y. Yue, S. Dolinar, M. Tur and A. E. Willner, "Terabit free-space data transmission employing orbital angular momentum multiplexing," Nat. Photonics, **6**, 488–496 (2012).

[8] N. Bozinovic, Y. Yue, Y. Ren, M. Tur, P. Kristensen, H. Huang, A. E. Willner, S. Ramachandran, "Terabit-scale orbital angular momentum mode division multiplexing in fibers," Science, **340**(6140), 1545–1548 (2013).

[9] G. Molina-Terriza, J. P. Torres and L. Torner, "Twisted photons," Nat. Phys., **3**(5), 305–310 (2007).

[10] I. Heller, G. Sitters, O. D. Broekmans, G. Farge, C. Menges, W. Wende, S. W. Hell, E. J. G. Peterman and G. J. L. Wuite, "STED nanoscopy combined with optical tweezers reveals protein dynamics on densely covered DNA," Nat. Methods, **10**(9), 910–916 (2013).

[11] T. Watanabe, Y. Iketaki, T. Omatsu, K. Yamamoto, M. Sakai and M. Fujii, "Two-point-separation in super-resolution fluorescence microscope based on up-conversion fluorescence depletion technique," Opt. Express, **11**(24), 3271 (2003).

[12] Y. Iketaki, T. Watanabe, S. Ishiuchi, M. Sakai, T. Omatsu, K. Yamamoto, M. Fujii, T. Watanabe, "Investigation of the fluorescence depletion process in the condensed phase; application to a tryptophan aqueous solution," Chem. Phys. Lett. **372**(5), 773–778 (2003).

[13] B. A. Parviz, D. Ryan and G. M. Whitesides, "Using self-assembly for the fabrication of nano-scale electronic and photonic devices," IEEE Trans. Adv. Packag., **26**(3), 233–241 (2003).

[14] S. Khumpuang, M. Horade, K. Fujioka and S. Sugiyama, "Microneedle fabrication using the plane pattern to cross-section transfer method," Smart Mater. Struct., **15**(2), 600–606 (2006).

[15] Y. Tang, A. E. Cohen, "Enhanced enantioselectivity in excitation of chiral molecules by superchiral light," Science, **332**(6027), 333–336 (2011).

[16] V. K. Valev, J. J. Baumberg, C. Sibilia, T. Verbiest, "Chirality and chiroptical effects in plasmonic nanostructures: fundamentals, recent progress and outlook," Adv. Mater., **25**, 2517–2534 (2013).

[17] T. Omatsu, K. Chujo, K. Miyamoto, M. Okida, K. Nakamura, N. Aoki, R. Morita, "Metal microneedle fabrication using twisted light with spin," Opt. Express, **18**(17), 17967–17973 (2010).

[18] P. Vettiger, M. Despont, U. Drechsler, U. Durig, W. Haberle, M. I. Lutwyche, H. E. Rothuizen, R. Stutz, R. Widmer and G. K. Binnig, "The "Millipede"—more than one thousand tips for future AFM data storage," IBM J. Res. Develop., **44**(3), 323–340 (2000).

[19] Q. H. Wang, A. A. Setlur, J. M. Lauerhaas, J. Y. Dai, E. W. Seelig and R. P. H. Chang, "A nanotube-based fieldemission flat panel display," Appl. Phys. Lett., **72**(22), 2912 (1998).

[20] L. Lin, A. P. Pisano, "Silicon-processed microneedles," J. Microelectromech. Syst., **8**(1), 78–84 (1999).

[21] D. V. McAllister, P. M. Wang, S. P. Davis, J-H Park, P. J. Canatella, M. G. Allen and M. R. Prausnitz, "Microfabricated needles for transdermal delivery of macromolecules and nanoparticles: fabrication methods and transport studies," PNAS, **100**(24), 13755–13760 (2003).

[22] E. Larrañeta, R. E. M. Lutton, A. D. Woolfson, R. F. Donnelly, "Microneedle arrays as transdermal and intradermal drug delivery systems: materials science, manufacture and commercial development," Mater. Sci. Eng. R: Rep., **104**, 1–32 (2016).

[23] S. Nolte, C. Momma, H. Jacobs, A. Tünnermann, B. N. Chichkov, B. Wellegehausen, H. Welling, "Ablation of metals by ultrashort laser pulses," J. Opt. Soc. Am. B, **14**(10), 2716–2722 (1997).

[24] X. Liu, D. Du, G. Mourou, "Laser ablation and micromachining with ultrashort laser pulses," IEEE J. Quantum Electron., **33**(10), 1716–1716 (1997).

[25] M. C. Gower, "Industrial applications of laser micromachining," Opt. Express, **7**(2), 56–67 (2000).

[26] J. Hamazaki, R. Morita, K. Chujo, Y. Kobayashi, S. Tanda, T. Omatsu, "Optical-vortex laser ablation", Opt. Express, **18**(3), 2144–2151 (2010).

[27] S.M. Barnett, "Optical angular momentum flux", J. Optics B Quantum Semiclassical Optics, **4**, S7–S16 (2002).

[28] A. T. O'Neil, I. MacVicar, L. Allen, M. J. Padgett, "Intrinsic and extrinsic nature of the orbital angular momentum of a light beam," Phys. Rev. Lett., **88**, 053601 (2002).

[29] M. W. Beijersbergen, R. P. C. Coerwinkel, M. Kristensen, J. P. Woerdman, "Helical-wavefront laser beams produced with a spiral phase plate," Opt. Commun., **112**(5–6), 321–327 (1994).

[30] F. Takahashi, K. Miyamoto, H. Hidai, K. Yamane, R. Morita, T. Omatsu, "Picosecond optical vortex pulse illumination forms a monocrystalline silicon needle," Sci. Rep., **6**, 21738, (2016).

[31] A. Blanco, E. Chomski, S. Grabtchak, M. Ibisate, S. John, S. W. Leonard, C. Lopez, F. Meseguer, H. Miguez, J. P. Mondia, G. A. Ozin, O. Toader and H. M. Driel1 "Large-scale synthesis of a silicon photonic crystal with a complete three-dimensional bandgap near 1.5micrometres," Nature **405**, 437–440 (2000).

[32] Y. A. Vlasov, X. Z. Bo, J. C. Sturm and D. J. Norris, "On-chip natural assembly of silicon photonic bandgap crystals," Nature **414**, 289–293 (2001).

[33] L. Hu and G. Chen, "Analysis of optical absorption in silicon nanowire arrays for photovoltaic applications," Nano Lett., **7**, 3249–3252 (2007).

[34] J. Bonse, S. Baudach, J. Krüger, W. Kautek, M. Lenzner, "Femtosecond laser ablation of silicon–modification thresholds and morphology," Appl. Phys. A, **74**, 19–25 (2002).

[35] J. Bonse, K. W. Brzezinka and A. J. Meixner, "Modifying single-crystalline silicon by femtosecond laser pulses: an analysis by micro Raman spectroscopy, scanning laser microscopy and atomic force microscopy," Appl. Surf. Sci., **221**, 215–230 (2004).

[36] A. B. Brailovsky, S. V. Gaponov and V. I. Luchin, "Mechanisums of melt droplets and solid-particle ejection from a target surface by pulsed laser action," Appl. Phys. A, **61**, 81–86 (1995).

[37] R. Evans, S. Camacho-López, F. G. Pérez-Gutiérrez, G. Aguilar, "Pump-probe imaging of nanosecond laser-induced bubbles in agar gel," Opt. Express, **16**(10), 7481–7492 (2008).

[38] K. Toyoda, K. Miyamoto, N. Aoki, R. Morita and T. Omatsu, "Using optical vortex to control the chirality of twisted metal nanostructures," Nano Lett., **12**, 3645–3649 (2012).

[39] K. Toyoda, F. Takahashi, S. Takizawa, Y. Tokizane, K. Miyamoto, R. Morita and T. Omatsu, "Transfer of light helicity to nanostructures," Phys. Rev. Lett., **110**, 143603 (2013).

[40] F. Takahashi, S. Takizawa, H. Hidai, K. Miyamoto, R. Morita and T. Omatsu, "Optical vortex pulse illumination to create chiral monocrystalline silicon nanostructures," Physica Status Solidi (a), **213**(4), 1063–1068, (2016).

[41] M. Park, M. Kim, J. Joo, K. Kim, J. Kim, S. Ahn, Y. Cui and J. Cho, "Silicon Nanotube Battery Anodes," Nano Lett., **9**(11), 3844 (2009).

[42] D. Zschech, D. Kim, A. P. Milenin, R. Scholz, R. Hillebrand, C. J. Hawker, T. P. Russell, M. Steinhart and U. Gösele, "Ordered arrays of <100>-oriented silicon nanorods by CMOS-compatible block copolymer lithography," Nano Lett., **7**(6), 1516 (2007).

[43] M. Watabe, G. Juman, K. Miyamoto and T. Omatsu, "Light induced conch-shaped relief in an azo-polymer film," Sci. Rep., **4**, 4281 (2014).

[44] A. Natansohn, P. Rochon, "Photoinduced motions in azo-containing polymers," Chem. Rev. **102**, 4139–4175 (2002).

[45] H. Ishitobi, M. Tanabe, Z. Sekkat, S. Kawata, "The anisotropic nanomovement of azo-polymers," Opt. Express, **15**, 652–659 (2007).

[46] N. K. Viswanathan, D. Y. Kim, S. Bian, J. Williams, W. Liu, L. Li, L. Samuelson, J. Kumar and S. K. Tripathy, "Surface relief structures on azo polymer films. J. Mater. Chem., **9**, 1941–1955 (1999).

[47] C. J. Barrett, A. L. Natansohn and P. L. Rochon, "Mechanism of optically inscribed high-efficiency diffraction gratings in azo polymer films," J. Phys. Chem., **100**, 8836–8842 (1996).

[48] A. Ambrosio, L. Marrucci, F. Borbone, A. Roviello, P. Maddalena, "Light-induced spiral mass transport in azo-polymer films under vortex-beam illumination," Nat. Commun., **3**, 989 (2012).

[49] K. Harada, H. Inoue, M. A. El-Morsy, M. Itoh, S. Umegaki, T. Yatagai, "Holographic recording and control of diffraction efficiency using photoinduced surface deformation on azo-polymer films," Jpn. J. Appl. Phys., **41**, 1851–1854 (2002).

[50] G. J. Fang, J. E. Maclennan, Y. Yi, M. A. Glaser, M. Farrow, E. Korblova, D. M. Walba, T. E. Furtak, N. A. Clark, "Athermal photofluidization of glasses," Nat. Commun., **4**, 1521 (2013).

[51] D. Barada, G. Juman, I. Yoshida, K. Miyamoto, S. Kawata, S. Ohno, T. Omatsu, "Constructive spin-orbital angular momentum coupling can twist materials to create spiral structures in optical vortex illumination," Appl. Phys. Lett., **108**, 051108 (2016).

[52] A. Ashkin, J. M. Dziedzic, J. E. Bjorkholm, S. Chu, "Observation of a single-beam gradient force optical trap for dielectric particles," Opt. Lett., **11**(5), 288–290 (1986).

[53] Y. Harada, T. Asakura, "Radiation forces on a dielectric sphere in the Rayleigh scattering regime," Opt. Commun., **124**, 529–541 (1996).

[54] A. Ambrosio, P. Maddalena, L. Marrucci, "Molecular model for light driven spiral mass transport in azopolymer films," Phys. Rev. Lett., **110**, 146102 (2013).

[55] J. Bin, W. S. Oates, "A unified material description for light induced deformation in azobenzene polymers," Sci. Rep., **5**, 14654 (2015).

[56] L. Marrucci, "Soft matter and optical vortices: A good match for new science and technology," Mol. Cryst. Liq. Cryst. **595**(1), 9–20 (2014).

IntechOpen